Physica B 654 (2023) 414738

Contents lists available at ScienceDirect

Physica B: Condensed Matter

journal homepage: www.elsevier.com/locate/physb

Thermoelectric transportation in Cu-added $Ca_3Co_4O_9$ ceramics consolidated by spark plasma sintering

Muhammad Umer Iqbal [a], Sumayya [a], Sajid Butt [b,*], Muhammad Umer Farooq [c], Shahid Hussain [d], Syed Irfan [e], Nazakat Ali [f], Muhammad Abdul Basit [a], Muhammad Aftab Akram [g], Muhammad Yasir [a], Ather Hassan [h]

[a] Department of Materials Science and Engineering, Institute of Space Technology, Islamabad, 44000, Pakistan
[b] Department of Space Science, Institute of Space Technology, Islamabad, 44000, Pakistan
[c] Department of Physics, University of Education (Lahore), Pakistan
[d] School of Materials Science and Engineering, Jiangsu University, Zhenjiang, 212013, China
[e] Shenzhen Key Laboratory of Advanced Thin Films and Applications, College of Physics and Optoelectronic Engineering, Shenzhen University, Shenzhen, 518060, China
[f] Office of Research, Inovation and Commercialization (ORIC), Institute of Space Technology, Islamabad, 44000, Pakistan
[g] Pak-Austria Fachhochschule: Institute of Applied Sciences, Department of Materials Science & Engineering, Mang, Khanpur Road, Haripur-KPK, Pakistan
[h] Department of Physics, Allama Iqbal Open University, Islamabad, Pakistan

ARTICLE INFO

Keywords:
Thermoelectric
Electrical conductivity
Transition metal oxides
SPS
$Ca_3Co_4O_9$

ABSTRACT

During the last decade, misfit layered calcium cobaltite ($Ca_3Co_4O_9$) has appeared as a potential candidate for oxide thermoelectric materials. In the present work, we report improved thermoelectric properties of $Ca_3Co_4O_9$ through a facile synthesis route. $Ca_3Co_4O_9$ based composites have been prepared by mixing different wt. % of Cu using ball-milling. The pure and composite powdered samples have been consolidated into bulk ceramics by spark plasma sintering (SPS). The detailed structural investigations reveal a multiphase system comprising of Cu, $Ca_3Co_4O_9$, $Ca_3Co_{4-x}Cu_xO_9$ and a minority phase of Co_3O_4. The simultaneous improvement in the electrical conductivity and Seebeck coefficient results in an improved power factor and the highest value of 384 μW/m.K^2 at 973K have been obtained for the sample containing 5% Cu by wt. The conduction mechanisms have been discussed in detail to investigate the reasons associated with the improved thermoelectric properties.

1. Introduction

Energy generation is mostly accomplished through the burning of fossil fuels, which results in releasing of harmful gases mainly carbon dioxide, which leads to global warming. Therefore, the paradigm is shifting towards alternate renewable energy sources. Currently, thermoelectric (TE) materials have gained immense importance for recycling waste heat into useful electricity and vice versa. The TE materials are used in various applications which are broadly classified into power generation- and solid-state refrigeration-modes [1–3]. The performance of any TE material is evaluated through a dimensionless figure-of-merit: $ZT = (\sigma S^2/k)T$, where, σ is electrical conductivity, S is Seebeck coefficient, k is total thermal conductivity, and T is working temperature, respectively. σS^2 is explicitly defined as power factor (PF). Thus ZT can be improved by increasing PF and decreasing k. For practical applications, TE materials having ZT value $\geq$ 1 are considered good thermoelectric materials [4].

The thermoelectric community has been working hard in search of environment-friendly, thermally stable, economically cheaper and promising TE transport properties in several classes of materials, for the last two decades [5]. Currently, chalcogenides such as PbSe [6,7], SnSe [8,9], $Cu_{2-x}Se$ [10–12], and Bi_2Te_3 [13] have shown great improvement in their thermoelectric properties. Furthermore, fine carrier tuning through elemental doping and novel nano-structuring have greatly boosted ZT values. For instance, mosaic crystals of $Cu_{2-x}Se$ have shown a higher ZT value of 2.2 [11]. Besides promising TE properties, thermal instability at higher temperatures in the air is another issue to be addressed before deploying these materials into industrial applications. Therefore, oxide TE materials have received immense importance from the thermoelectric community due to their thermal stability, non-toxicity and in addition to their cost-effective and easy processing routes [14]. Thus various oxide materials like ZnO [15], $SrTiO_3$ [16],

* Corresponding author.
E-mail address: sajid.butt@ist.edu.pk (S. Butt).

https://doi.org/10.1016/j.physb.2023.414738
Received 14 October 2022; Received in revised form 26 December 2022; Accepted 25 January 2023
Available online 10 February 2023

BiCuSeO [17,18], $LaCoO_3$ [19], $SmBaCuFeO_5$ [20], $Ca_3Co_4O_9$ [21] along with some other materials have been investigated for better TE properties [22–26]. Funahashi et al. have reported higher TE performance of single-crystalline $Ca_2Co_2O_5$, where the single crystalline whiskers have shown a higher *ZT* from 1.2 to 2.7 in the air from a temperature range of 473–973 K [27]. Contrarily, the polycrystalline $Ca_2Co_2O_5$ (Co-225) exhibits a lower *ZT* value of 0.21 due to lower electrical conductivity as compared to its single crystalline counterpart [28].

Among the oxide thermoelectric materials, misfit-layered calcium cobaltite: $Ca_3Co_4O_9$ (CCO) has received particular attention owing to its unique crystal structure. CCO is comprised of a natural superlattice structure consisting of two subsystems i.e., Ca_2CoO_3 as rock salt insulating layers and CoO_2 as CdI_2-conductive layers stacked alternatively along the c-axis direction. These two subsystems have monoclinic structures sharing the same values for parameters *a*, *c* and β but having different lattice parameter *b*, which makes CCO misfit-layered structure along *b* axis [17]. This high structural anisotropy played a crucial role in enhancing the thermoelectric properties of materials. In single-crystalline CCO, the *ZT* value reaches ~1 [29], however, the polycrystalline CCO, the *ZT* value is lower. Several researchers have outlined the different strategies for the enhancement of TE performance in polycrystalline CCO, such as novel nano-structuring [30,31], elemental doping [32–37], and composite formation [38–41]. Among the reported methods, Bi-doped CCO: ($Ca_{2.8}Bi_{0.2}Co_4O_9$) has shown an increased *ZT* value of 0.43 at 1073 K [41]. The excessive Bi is segregated at grain boundaries, which acts as a carrier filter for lowering the thermal conductivity. Similar effects of carrier filtering and crystal texture improvement were found in Ba doped CCO, where Ba was also segregated at the grain boundaries, and *ZT* was greatly enhanced to 0.52 [42]. The simultaneous dual doping of Bi and Ba at the Ca site in CCO has further improved TE properties as reported by Boyle et al. [43]. Similarly, Zn doping at the Co-site in the rock-salt layer of CCO has increased carriers concentration which results in an improved electrical conductivity and thus *ZT* [44]. Another study on doping of Ag at the Ca site along with the segregation of the Ag phase has increased TE properties [45,46]. Further, Cu-doping at Co-site has been reported to increase the thermoelectric properties [39 47,48].

Though, the mechanism of elemental Cu on the TE properties of CCO has not been investigated earlier. So, in the present work, Cu-based CCO composites have been prepared through planetary ball milling followed by consolidation into bulk by spark plasma sintering, to inquire about the effect of Cu addition on CCO's TE transport properties.

2. Experimental design

2.1. Materials and methods

Pure $Ca_3Co_4O_9$ (CCO) was synthesized through the sol-gel method, as illustrated in Fig. 1, using reagent grade metal precursors and citric acid. The stoichiometric amounts of $Ca(NO_3)_2{\cdot}4H_2O$ and $Co(NO_3)_2{\cdot}6H_2O$ were dissolved into distilled water and then required citric acid in a molar ratio of metal ions: citric acid ≈1.5, as a chelating agent, was also added. The obtained solution was stirred for 3 h at 80 °C to form a homogenous solution. The obtained solution was placed in an oven at 130 °C overnight. The obtained dried spongy gel was ground to fine powder followed by calcination at 800 °C for 8 h in the presence of air. The resultant product was again grounded to a fine powder. For the synthesis of Cu-based CCO composites, 5 wt% and 10 wt% of elemental Cu (99.9%) powder was mixed into as-synthesized CCO through Ball milling for 2 h in an ethanol medium. The obtained slurries were dried and thoroughly mixed again with the pestle and mortar to get homogeneous compositions. The obtained pure and composite specimens were consolidated into bulk ceramics by spark plasma sintering (SPS) at 750 °C for 5 min and under a uniaxial pressure of 50 MPa, in the presence of an inert atmosphere. The obtained pellets were then cut into rectangular bars having dimensions 3 × 3x15 mm^3 to be used for the determination of thermoelectric properties.

Phase purity and crystal structure were determined by X-rays diffraction (XRD) pattern using Cu Kα radiations (λ = 0.15406 nm) with XRD: Rigaku. Scanning Electron Microscopy (SEM: TESCAN Mira-3) coupled with energy-dispersive spectroscopy (EDS) was used to examine grain morphology and elemental composition. The temperature-dependent electrical conductivity and Seebeck coefficient were measured simultaneously on a home-made computer-controlled apparatus (equipped with Agilent 34420A and Agilent 6612C meters) [41]. For the determination of electronic thermal conductivity with the aid of the Wiedemann-Franz law, the Lorenz number (*L*) values were estimated using the single parabolic band (SPB) model.

3. Results and discussion

3.1. Structural properties

The crystal structure of pure and Cu-based $Ca_3Co_4O_9$ (CCO) composite phases i.e., Cu-5% and Cu-10% was determined through XRD patterns, as shown in Fig. 2. It can be seen that the XRD pattern of pure

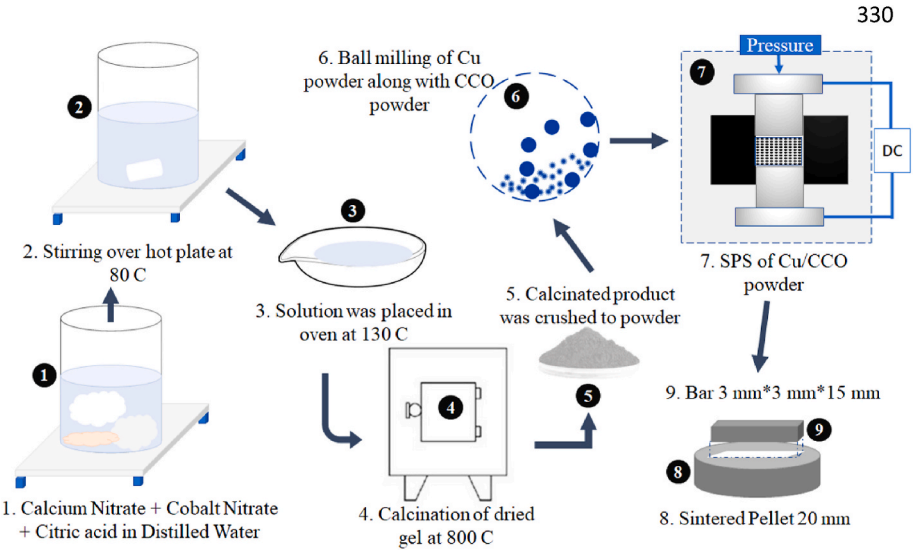

Fig. 1. Schematic of step-by-step synthesis of pure CCO and Cu-based composites through sol-gel followed by SPS.

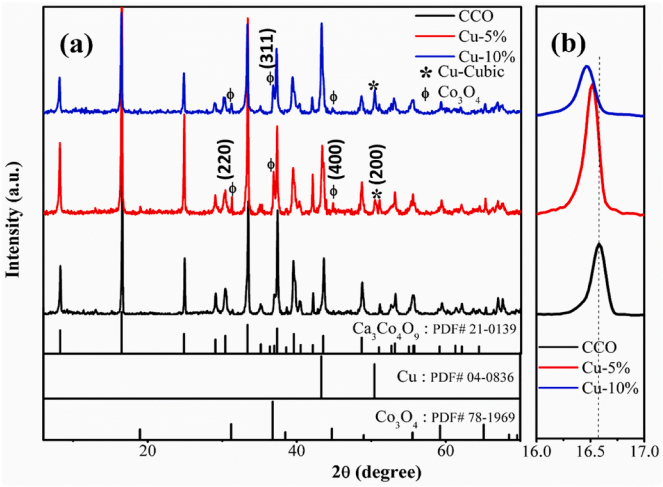

Fig. 2. XRD patterns of pure and Cu-based composites of $Ca_3Co_4O_9$ **(a)**, and peak shift appeared due to partial doping of Cu into the lattice **(b)**.

CCO is indexed to PDF # 21–0139, which reveals the purity of CCO up to the detectable limit of XRD. However, for the composite phases, all the specimens possessed the predominant phase of CCO and the presence of secondary phases i.e., pure Cu as indexed by PDF # 04–0836 and Co_3O_4 as indexed by PDF # 78–1969. With these secondary phases, the emergence of a few new diffraction peaks was observed, which were intensified as Cu contents were increased from 5% to 10%. On the other hand, a small peak shift towards lower 2θ for both composite samples demonstrates partial substitution of Cu into the lattice of CCO. For Cu-10%, a slightly higher peak shift is observed, which represents a higher partial substitution of Cu into the lattice of CCO as compared to that of Cu-5%. The possibility of doping of Cu at Ca-sites is neglected because of the high difference in the ionic radii of Ca and Cu. Thus, based upon very small difference in ionic radii of Cu and Co, it can be concluded that Cu is partially substituted at Co-sites. As the Cu ion is little larger in ionic radius than Co ion, which induces tensile stress in the crystal lattice and as a result the XRD patterns were shifted towards lower 2 θ values [47,48]. The lattice parameters were determined from XRD patterns using the least-square refinement method, as shown in Table 1. With the increase in Cu content, a slight increase in all the lattice parameters is observed, especially in b_1 and b_2, which indicates that Cu substitutes partially into both layers and generates tensile stress.

To determine phase distributions, the back-scattered electron (BSE) images and EDS area mapping were performed, as shown in Fig. 3(a–e). Freshly broken pellets were polished to study the different phases and their distribution in the Cu/CCO composites. The back-scattered electron (BSE) image taken for the Cu-10% sample reveals that the composite samples are comprised of two-phase system represented by bright and dark contrast regions, as shown in Fig. 3(a). The bright and dark areas are corresponding to Cu CCO phases, respectively, as the atomic mass of Cu is greater than the average atomic mass of CCO. Furthermore, the EDS mapping of the Cu-10% sample as shown in Fig. 3(b–e), also validates the conclusion drawn by the BSE image that bright and dark regions, respectively, represent Cu and CCO. Secondly, the XRD analysis has also confirmed the presence of pure Cu phase along with Cu-doped CCO for the Cu-10% sample. Therefore, based on these structural characterizations, it is concluded that Cu doped CCO along with the elemental Cu phases has been formed.

Table 1
Cell parameters of pure CCO and Cu/CCO composites determined through the XRD data, where b_1 and b_2 belong to the rock salt-type and conductive-type layers, respectively.

Sr.No	*a* (Å)	b_1 (Å)	*c* (Å)	*β*	b_2 (Å)	b_1/b_2
CCO	4.827	4.561	10.833	97.67	2.820	1.618
Cu 5%	4.831	4.568	10.835	97.99	2.820	1.620
Cu 10%	4.827	4.568	10.836	97.85	2.823	1.618

3.2. Thermoelectric transport properties

The temperature dependent electrical conductivity (σ) of pure CCO and composite phases (Cu-5%, and Cu-10%) has been measured as shown in Fig. 4 (a). For all the series of samples, an increase in the electrical conductivity upon increasing temperature has been obtained, which confirms a semiconducting behavior of samples. The semiconducting behavior is more prominent for the Cu/CCO composites as compared to pure CCO. Secondly, a sudden change in the slopes of curves above 573 K can be observed owing to the transition of the spin state of Co in CCO [49–53]. Magnetic and electrical anomalies around 573 K mainly occurred due to the change in the magnetic moment of Co ions, which was reported earlier by Heikes et al. [50]. Later on, Yamaguchi et al. [51] and Abbate et al. [52] validated the spin-state transition of Co-ions in $LaCoO_3$. The confinement of magnetic polarons with high spin values (S = 10–16) triggered due to the interaction of holes with low spin state Co-ions in $LaCoO_3$ has been reported [51]. The effect of doping and temperature on the spin state of Co-ions in CCO has also shown similar shifts from low to high spin numbers at higher temperatures [54–56].

The electrical conductivity measured for pure CCO is 77.97 S/cm at 323 K, which is superior to that of Cu/CCO composites at this temperature. With an increase of Cu contents in the CCO-composites, the electrical conductivity decreases but the highest electrical conductivity among all the samples was achieved for Cu-5% i.e., 90.74 S/cm at 973 K. This increase in the electrical conductivity of Cu-5% at higher temperature is associated with the doping of Cu at Co-site increases carriers concentration and small polaron hopping in CCO at higher temperatures. Here, in the present report, a notable decrease in σ by Cu addition is contrary to the previous reports on Cu-doped CCO, in which Cu substitution at the Co-site of Ca_2CoO_3 layer in CCO has been reported to enhance σ by increasing carriers concentration [39,47,48]. However, in the present case, the reduction of σ may be associated with different reasons, but mainly due to the formation of the Co_3O_4 phase as confirmed by XRD (Fig. 2), which is a less conductive phase as compared to CCO. The σ of Co_3O_4 and some transition metal-doped Co_2O_3 lies between 0.1 and 10^{-4} S/cm, which is very low compared to that of CCO [57–61]. F. Delorme et al. found a reduced σ in the composite of CCO and Co_3O_4 due to the lower intrinsic electrical conductivity of Co_3O_4 than that of CCO [62]. However, in the present case, the partial substitution of Cu at the Co site in the lattice of CCO along with the formation of Co_3O_4 was confirmed by XRD results, as shown in Fig. 1 (a&b). In CCO, the electrical conduction is accompanied mainly by CoO_2 layers, while Ca_2CoO_3 rock-salt layers act as a reservoir of charge carriers. However, the partial substitution of Cu in CoO_2 acts as strong scattering regions, which can reduce the overall σ by fluctuating the electrical pathways, as reported earlier [32]. Thus based upon XRD and electrical conductivity data, it is inferred that for a lower concentration of Cu (Cu 5%), it first enters into Ca_2CoO_3 rock-salt layers where it increases electrical conductivity by increasing carriers concentration especially at higher temperatures, however, upon the further increase in Cu (Cu 10%), it starts entering into CoO_2 layers which lower electrical conductivity by introducing scattering site.

Fig. 4 (b) shows modified Arrhenius plots of ln (σ.T) vs. 1000/T, in which linear fitting of the curve shows two regions i.e., low and high-temperature regions from 323 K to 573 K and onwards as represented by dotted and solid lines, respectively. Transport properties of carriers are dominated by the hopping of small polaron at higher temperatures in metal oxide like CCO [63]. The linear fitting in Fig. 4 (b) shows the conduction mechanism in this work is also accompanied by hopping the small polaron model, which is represented by the following equation as:

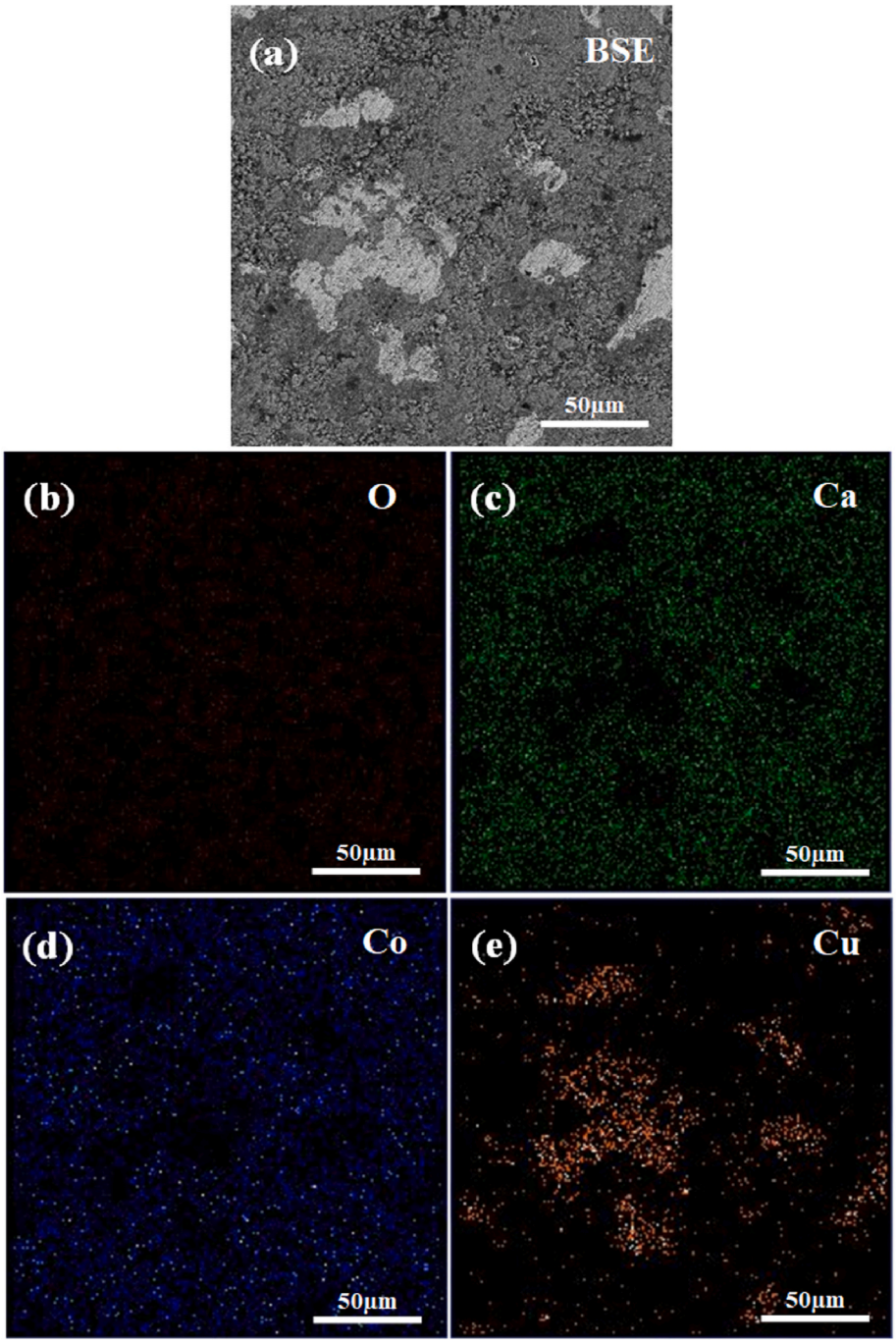

Fig. 3. Backscattered electron (BSE) images of Cu-10% **(a)** along with elemental distribution taken by energy dispersive spectroscopy (EDS) **(b–e)**.

$$\sigma = \sigma_o \exp\left(\frac{-Ea}{K_B T}\right) \quad (1)$$

where E_a is the activation energy, K_B is Boltzmann constant, T is the absolute temperature, and σ_o is given by;

$$\sigma_o = nea^2\left(\frac{A}{T}\right) \quad (2)$$

here n, e, a, and A are carriers concentration, electronic charge, inter-site hopping distance, and pre-exponential term associated with the scattering mechanism.

The activation energy was determined from the slopes of the fitted line obtained by Arrhenius plots. The high and low-temperature regions i.e., from 323 K to 573 K and from 573 K to 973 K are characterized by their activation energies E_{a1} and E_{a2}, respectively. The relation between activation energy and electrical conductivity is usually inverse; this trend is found in several oxides and inorganic materials, as reported earlier, where lower electrical conductivity is found with higher activation energy [64–66]. At higher temperatures, higher activation energy is required for the conduction of carriers. Table 2 shows that the activation energy E_{a1} of the carriers was increased with the increase of Cu in the CCO/Cu composites in the lower temperature range, whereas this increase in activation energy may be associated with the rise of carriers scattering. The activation energy in the higher temperature range also increases with the addition of Cu, but the increasing trend of E_{a2} is much higher than that of E_{a2}. Cu-10% has the highest activation energy at lower and higher temperature ranges as the scattering of carriers shows

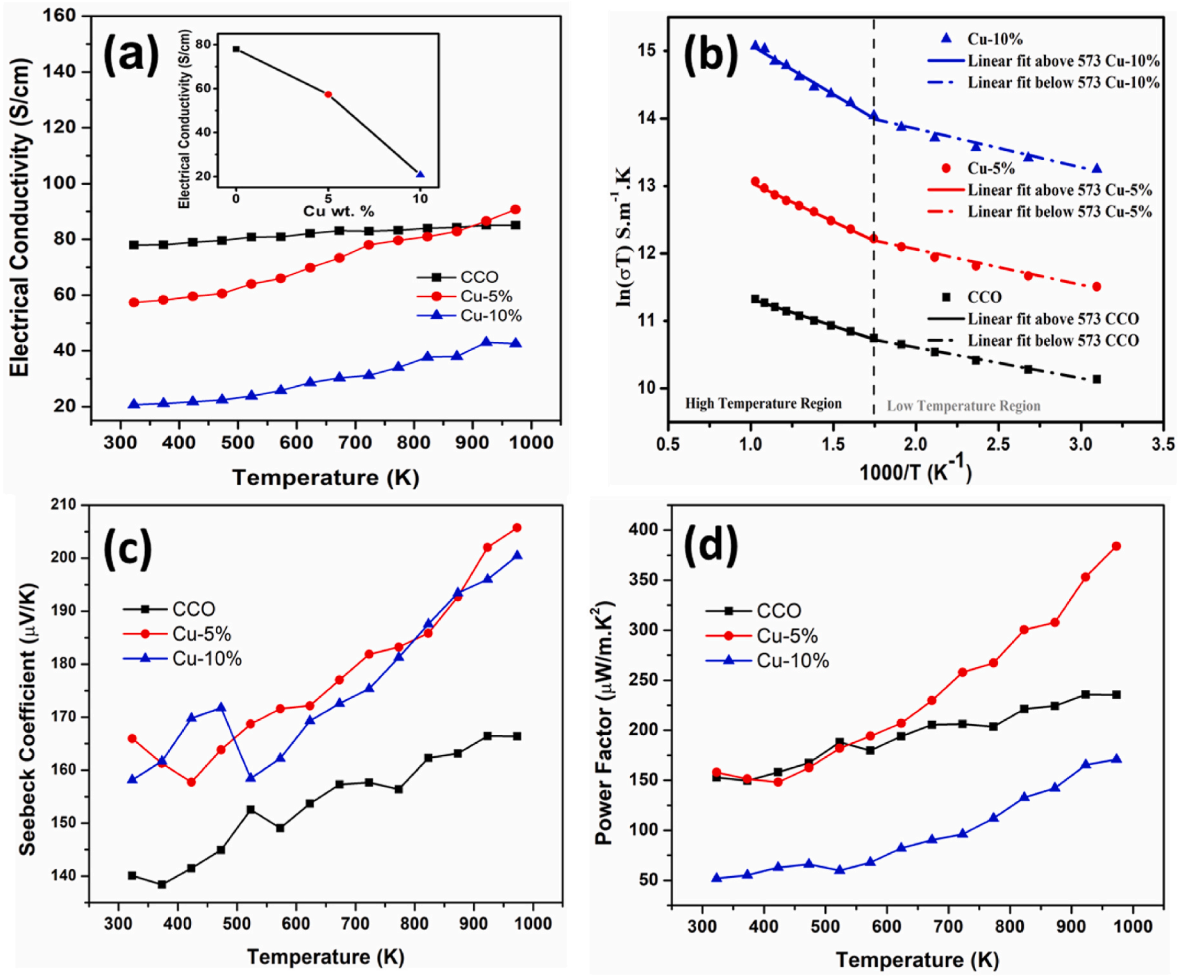

Fig. 4. Temperature dependence of thermoelectric properties of pure CCO and composite phase (Cu-5%, Cu-10), (a) Electrical Conductivity, inset graph represents Electrical Conductivity VS Cu wt % (b) Activation Energy, (c) Seebeck Coefficient and (d) Power Factor.

Table 2
The activation energies E_{a1} and E_{a2} are associated to low temperature (323 K–573 K) and high temperature (573 K–973 K) regions, respectively.

Sr.no	E_{a1} (meV)	E_{a2} (meV)
CCO	39.1	69.3
Cu-5%/CCO-95%	45.1	99.4
Cu-10%/CCO-90%	49.2	125.6

much increase and hole transportation becomes more difficult mainly due to the formation of the least conductive phase i.e., Co_3O_4 and by the partial substitution of Cu in conductive CoO_2 layer of CCO by prevents carriers transportation and acts as strong carrier scattering regions which suppress the small polaron hopping by localization of charges. The results obtained for Cu/CCO are consistent with the data reported by Yao et al. for which a sharp decrease in polaron hopping of carriers was observed by the partial substitution of Mn at Co-sites in CoO_2 layers, which resulted in strong charge localization and decreased the electrical conductivity and increased the activation energy and Seebeck coefficient [28].

The temperature-dependent Seebeck coefficient (S) was measured for all the pure and composite samples from 323 to 973 K, as shown in Fig. 4 (c). A positive S value was obtained for all the samples, which confirms their p-type semiconducting behavior. For all the composite samples, S increased considerably as compared to that of pure CCO. A higher S value of 206 μV/K was obtained at 973 K for Cu-5%. The increase in S for Cu-5% is almost 20% higher than that of pure CCO. However, the further rise in Cu content into CCO, results in a decreased S value for Cu-10%. These results are consistent with the reported data on $NaCo_{1.7}Cu_{0.3}O_4$ [67].

For the composite samples, Cu substitution mainly influenced by the concentration of Co^{+4} in CCO. The relation between Seebeck coefficient (S) and the concentration of Co^{+4} is described by the modified Heike formula as given below;

$$S = -\frac{K_B}{e}\left[\frac{g_3}{g_4}\left(\frac{c}{1-c}\right)\right] \quad (3)$$

where K_B/e is constant, c is the concentration of Co^{+4}, g_3, and g_4 are the spin-orbital degeneracy of Co^{+3} and Co^{+4}, respectively. It is concluded from the above expression that S is influenced by the spin-orbital degeneracy ratio (g_3/g_4) and can be enhanced by decreasing the concentration of Co^{+4}. Spin entropy contribution can be disturbed by the substitution of elements in CCO, as it was previously concluded to increase S in Cd, Ba and Pb doped CCO [17,30]. Similarly, here in the present case, the partial substitution of Cu at Co-sites in CCO layers might have increased the spin entropy by decreasing the concentration of Co^{+4} which results in an increased S value. S of Cu-10% shows increases due to higher scattering at lower temperature range and then a slight decrease above 500 K, where the reduction in S up to 3% at 973 K in Cu-10% as compared to that of Cu-5% is observed due to agglomeration of Cu, which bypasses thermoelectric voltage between the cobaltite grains and decreases the S slightly. This result is consistent with the phenomenon revealed in Ag/CCO composites, where Ag in

between the cobaltite grains either has little effect on S or considerably degrades S by nullifying the thermoelectric voltage [38,40]. Thus the presence of Cu as a metallic phase can degrade S significantly. However, this suppression was minimal, and Cu-10% still possesses higher S values than that of pure CCO due to the higher scattering of carriers and spin entropy contribution.

The power factor (PF): $S^2\sigma$ of pure CCO and Cu/CCO composites was calculated from measured values of S and σ and, as shown in Fig. 4(d). The PF is increased with increasing temperature for all the samples. The highest PF value of 384 μW/m.K^2 at 973 K has been achieved for Cu-5%, which is about 63% higher than that of pure CCO. This promising increase is associated with a simultaneous increase in the S and σ. Among all the samples, Cu-10% has the lowest PF values throughout the temperature range due to a prevalent decrease in the σ.

The electronic thermal conductivity (K_{hole}) was estimated through Wiedemann-Franz law as given:

$$K_{hole} = L_o \sigma T \tag{4}$$

where L_o, σ and T are Lorentz constant, electrical conductivity, and absolute temperature, respectively. The constant value of 2.44×10^{-8} W Ω/K^2 used for L_o in research, is valid only for metal-like materials having low S values and deviates up to 40% from the estimated values for semiconductors having S greater than 50 μV/K. Single parabolic band (SPB) with acoustic phonon scattering (APS) can be used for getting more accurate values of Lorentz number with its limitation of unsuitability to explain bipolar transport [68]. However, here positive values of S demonstrate that the majority of charge carriers for electronic transport are holes in the Cu/CCO composites, and therefore SPB-APS model has been used to approximate the Lorentz number values (L) with minimal error. For a list of Seebeck coefficient (S) values, a list of Lorenz values (L) was calculated by solving the following expressions.

$$L = \left(\frac{k_B}{e}\right)^2 \left[\frac{(r+\frac{7}{2})F_{r+\frac{5}{2}}(\varepsilon)}{(r+\frac{3}{2})F_{r+\frac{1}{2}}(\varepsilon)} - \frac{(r+\frac{5}{2})F_{r+\frac{3}{2}}(\varepsilon)}{(r+\frac{3}{2})F_{r+\frac{1}{2}}(\varepsilon)}\right] \tag{5}$$

where r and ε are the carriers scattering factor and reduced chemical potential, respectively, and $F_n(\varepsilon)$ is a Fermi integral represented as:

$$F_n(\varepsilon) = \int_0^\infty \frac{x^n}{1+e^{1-\varepsilon}} dx \tag{6}$$

here ε can be calculated by the following expression through the values of Seebeck coefficient (S) and carriers scattering parameters (r):

$$S = \pm \frac{k_B}{e}\left[\frac{(r+\frac{5}{2})F_{r+\frac{3}{2}}(\varepsilon)}{(r+\frac{3}{2})F_{r+\frac{1}{2}}(\varepsilon)} - \varepsilon\right] \tag{7}$$

The estimated values of L as a function of ε and r are shown in Fig. 5 (a), in which a large deviation in L can be observed from the degenerate limit (2.44×10^{-8} W Ω/K^2).

k_{hole} was estimated from Eq. (4) using L as calculated by the SPB-APS model and is shown in Fig. 5 (b), in which k_{hole} shows similar increasing trends as that of σ data.

4. Conclusions

Pure and Cu-added $Ca_3Co_4O_9$ (CCO) ceramic samples were prepared through a sol-gel route followed by subsequent sintering using spark plasma sintering (SPS). The composite samples contain Cu and the least conductive Co_3O_4 as a secondary phase within the $Ca_3Co_4O_9$ matrix. The secondary phases were increased with increasing content of Cu, which decreases the σ due to increased carriers scattering. However, the partial doping of copper in Cu-5% composite showed an increase in σ at higher temperatures due to an increase of carriers concentration and the highest σ of 90.74 S/cm was achieved for Cu-5% at 973 K. In Cu-10% composite, scattering of carriers was dominant at lower temperature and polaron hopping conduction was also suppressed by strong charge localization due to an increase in Cu and Co_3O_4 phases and partial substitution of Cu into CoO_2 layers of CCO. On the other hand, S was greatly improved by the addition of Cu in CCO and possessed positive values confirming p-type semiconductor characteristics. The highest S of 206 μV/K was achieved for Cu-5%; higher S values in Cu-5% are mainly due to the partial doping of Cu at the Co-site which enhanced spin entropy contribution. Lorenz number values were calculated using a single parabolic band (SPB) coupled with an acoustic phonon scattering (APS) condition. Electronic thermal conductivity (k_{hole}) follows the same trend as that of electrical conductivity.

The effect of Cu addition in CCO sheds light on the future enhancement of carriers transport properties of CCO, which can be done through reaction-assisted compositing of CCO with any other transition metal that can form secondary phase of higher electrical conductivity along with partial cationic doping.

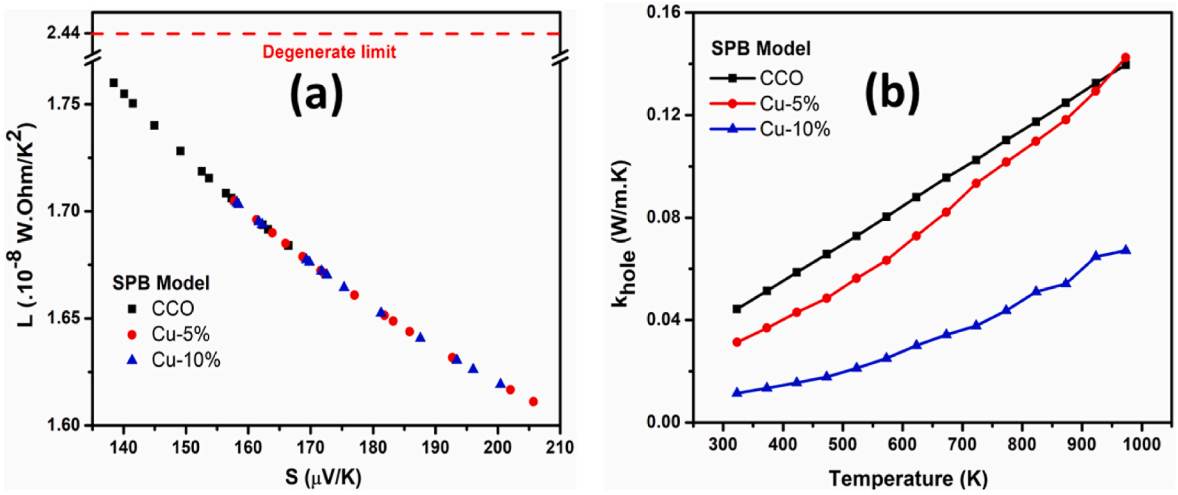

Fig. 5. Estimation of (a) Lorentz number through single parabolic band (SPB) and acoustic phonon scattering (APS) and (b) electronic thermal conductivity of pure CCO and Cu/CCO composites.

Credit author statement

Muhammad Umer Iqbal: Experiment and Write up of draft; Sumayya: Plotting of Data, Proofread; Sajid Butt: Methodology, Experiment, Supervision; Muhammad Umer Farooq: Reviewing and Editing; Shahid Hussain: Reviewing and Editing; Syed Irfan: Validation of Results; Nazakat Ali: Reviewing and Editing; Muhammad Abdul Basit: Visualization; Muhammad Aftab Akram: Reviewing and Editing; Muhammad Yasir: Materials and Design; Ather Hassan: Reviewing and Editing.

Declaration of competing interest

The authors declare that they have no known competing financial interests or personal relationships that could have appeared to influence the work reported in this paper.

Data availability

Data will be made available on request.

Acknowledgments

The authors are thankful to the Higher Education Commission (HEC) of Pakistan for financial support through the project: 8096/Federal/NRPU/R&D/HEC/2017. The authors are also thankful to Tsinghua University China for providing technical assistance.

References

[1] X. Liu, Y.D. Deng, Z. Li, C.Q. Su, Performance analysis of a waste heat recovery thermoelectric generation system for automotive application, Energy Convers. Manag. 90 (2015) 121–127.
[2] C. Hadjistassou, E. Kyriakides, J. Georgiou, Designing high efficiency segmented thermoelectric generators, Energy Convers. Manag. 66 (2013) 165–172.
[3] G.J. Snyder, A.H. Snyder, Figure of merit ZT of a thermoelectric device defined from materials properties, Energy Environ. Sci. 10 (2017) 2280–2283.
[4] M.S. Dresselhaus, G. Chen, M.Y. Tang, R.G. Yang, H. Lee, D.Z. Wang, Z.F. Ren, J. P. Fleurial, P. Gogna, New directions for low-dimensional thermoelectric materials, Adv. Mater. 19 (2007) 1043–1053.
[5] S. Johnsen, J. He, J. Androulakis, V. P Dravid, I. Todorov, D.Y. Chung, M. G. Kanatzidis, Nanostructures boost the thermoelectric performance of PbS, J. Am. Chem. Soc. 133 (2011) 3460–3470.
[6] L.D. Zhao, S.H. Lo, Y. Zhang, H. Sun, G. Tan, C. Uher, C. Wolverton, V.P. Dravid, M. G. Kanatzidis, Ultralow thermal conductivity and high thermoelectric figure of merit in SnSe crystals, Nature 508 (2014) 373–377.
[7] S. Butt, M.U. Farooq, W. Mahmood, S. Salam, M. Sultan, M.A. Basit, J. Ma, Y. Lin, C.W. Nan, One-step rapid synthesis of Cu_2Se with enhanced thermoelectric properties, J. Alloys Compd. 786 (2019) 557–564.
[8] J.L. Lan, Y.C. Liu, B. Zhan, Y.H. Lin, B. Zhang, X. Yuan, W. Zhang, W. Xu, C.W. Nan, Enhanced thermoelectric properties of Pb-doped BiCuSeO ceramics, Adv. Mater. 25 (2013) 5086–5090.
[9] J. Liang, H. Yang, C. Liu, L. Miao, J. Chen, S. Zhu, Z. Xie, W. Xu, X. Wang, J. Wang, B. Peng, K. Koumoto, Realizing a high ZT of 1.6 in n-type Mg_3Sb_2-based zintl compounds through Mn and Se codoping, ACS Appl. Mater. Interfaces 12 (2020) 21799–21807.
[10] L. Hu, T. Zhu, X. Liu, X. Zhao, Point defect engineering of high-performance Bismuth-Telluride-based thermoelectric materials, Adv. Funct. Mater. 24 (2014) 5211–5218.
[11] Y. He, P. Lu, X. Shi, F. Xu, T. Zhang, G.J. Snyder, C. Uher, L. Chen, Ultrahigh thermoelectric performance in mosaic crystals, Adv. Mater. 27 (2015) 3639–3644.
[12] D.B. Zhang, H.Z. Li, B.P. Zhang, D.D. Liang, M. Xia, Hybrid-structured ZnO thermoelectric materials with high carrier mobility and reduced thermal conductivity, RSC Adv. 7 (2017) 10855–10864.
[13] P.P. Shang, B.P. Zhang, Y. Liu, J.F. Li, H.M. Zhu, Preparation and thermoelectric properties of La-doped $SrTiO_3$ ceramics, J. Electron. Mater. 40 (2011) 926–931.
[14] M.U. Farooq, S. Butt, K. Gao, Y. Zhu, X. Sun, X. Pang, S.U. Khan, F. Mohmed, A. Mahmood, N. Mahmood, W. Xu, Cd-doping a facile approach for better thermoelectric transport properties of BiCuSeO oxyselenides, RSC Adv. 6 (2016) 33789–33797.
[15] Y. Wang, F. Li, L. Xu, Y. Sui, X. Wang, W. Su, X. Liu, Large thermal conductivity reduction induced by La/O vacancies in the thermoelectric $LaCoO_3$ system, Inorg. Chem. 50 (2011) 4412–4416.
[16] C. Zeng, S. Butt, Y.H. Lin, M. Li, C.W. Nan, Enhanced thermoelectric performance of $SmBaCuFeO_{5+\delta}$/Ag composite ceramics, J. Am. Ceram. Soc. 99 (2016) 1266–1270.
[17] S. Butt, W. Xu, W.Q. He, Q. Tan, G.K. Ren, Y. Lin, C.W. Nan, Enhancement of thermoelectric performance in Cd-doped $Ca_3Co_4O_9$ via spin entropy, defect chemistry and phonon scattering, J. Mater. Chem. 2 (2014) 19479–19487.
[18] K. Koumoto, Y. Wang, R. Zhang, A. Kosuga, R. Funahashi, Oxide thermoelectric materials: a nanostructuring approach, Annu. Rev. Mater. Res. 40 (2010) 363–394.
[19] G. Ren, J. Lan, C. Zeng, Y. Liu, B. Zhan, S. Butt, Y.H. Lin, C.W. Nan, High performance oxides-based thermoelectric materials, JOM 67 (2015) 211–221.
[20] R. Funahashi, I. Matsubara, H. Ikuta, T. Takeuchi, U. Mizutani, S. Sodeoka, An oxide single crystal with high thermoelectric performance in air, Jpn. J. Appl. Phys. 39 (2000) 1127–1129.
[21] Y. Zhang, J. Zhang, Q. Lu, Rapid synthesis of $Ca_2Co_2O_5$ textured ceramics by coprecipitation method and spark plasma sintering, J. Alloys Compouds 399 (2005) 64–68.
[22] M. Shikano, R. Funahashi, Electrical and thermal properties of single-crystalline $(Ca_2CoO_3)_{0.7}CoO_2$ with a $Ca_3Co_4O_9$ structure, Appl. Phys. Lett. 82 (2003) 1851–1853.
[23] Y. Miyazaki, Crystal structure and thermoelectric properties of the misfit-layered cobalt oxides, Solid State Ionics 172 (2004) 463–467.
[24] I. Haq, J. Jacob, K. Mehboob, K. Mahmood, A. Ali, N. Amin, S. Ikram, S. Hussain, Y. Feng, F. Ashraf, Effect of annealing temperature on the thermoelectric properties of ZnInO thin films grown by physical vapor deposition, Physica B: Condens. Matter Phys. 606 (2021), 412569.
[25] M. Shakil, S. Mushtaq, I. Zeba, S.S.A. Gillani, M.I. Khan, H. Arshad, M. Rafique, Structural, electronic, magnetic and thermoelectric properties of full heusler alloys Co2YZ (Z = S, Ge, Se): a first principles calculation, Physica B: Condens. Matter Phys. 602 (2021), 412558.
[26] Z. Tanveer, K. Mahmood, S. Ikram, A. Ali, N. Amin, Modulation of thermoelectric properties of thermally evaporated copper nitride thin films by optimizing the growth parameters, Physica B: Condens. Matter Phys. 605 (2021) 412.
[27] H.W. Eng, W. Prellier, S. Hébert, D. Grebille, L. Méchin, B. Mercey, Influence of pulsed laser deposition growth conditions on the thermoelectric properties of $Ca_3Co_4O_9$ thin films, J. Appl. Phys. 97 (2004), 013706.
[28] Q. Yao, D.L. Wang, L.D. Chen, X. Shi, M. Zhou, Effects of partial substitution of transition metals for cobalt on the high-temperature thermoelectric properties of $Ca_3Co_4O_{9+\delta}$, J. Appl. Phys. 97 (2005), 103905.
[29] Y. Wang, Y. Sui, J. Cheng, X. Wang, W. Su, Comparison of the high temperature thermoelectric properties for Ag-doped and Ag-added $Ca_3Co_4O_9$, J. Alloys Compd. 477 (2009) 817–821.
[30] S. Butt, Y. Ren, M.U. Farooq, B. Zhan, R.U.R. Sagar, Y. Lin, C.W. Nan, Enhanced thermoelectric performance of heavy-metals (M: Ba, Pb) doped misfit-layered ceramics: $(Ca_{2-x}M_xCoO_3)_{0.62}$ (CoO_2), Energy Convers. Manag. 83 (2014) 35–41.
[31] S. Butt, Y.C. Liu, J.L. Lan, K. Shehzad, B. Zhan, Y. Lin, C.W. Nan, High- temperature thermoelectric properties of La and Fe Co-doped Ca–Co–O misfit- layered cobaltites consolidated by spark plasma sintering, J. Alloys Compd. 588 (2014) 277–283.
[32] S.F. Wang, Y.F. Hsu, J.H. Chang, S. Cheng, H.C. Lu, Characteristics of Cu and Mo-doped $Ca_3Co_4O_{9-\delta}$ cathode materials for use in solid oxide fuel cells, Ceram. Int. 42 (2016) 11239–11247.
[33] T. Sun, H.H. Hng, Q.Y. Yan, J. Ma, Effect of Ag-doping on crystal structure and high temperature thermoelectric properties of c-axis oriented $Ca_3Co_4O_9$ thin films by pulsed laser deposition, J. Alloys Compd. 511 (2012) 133–138.
[34] G. Constantinescu, S. Rasekh, M.A. Torres, J.C. Diez, M.A. Madre, A. Sotelo, Effect of Sr substitution for Ca on the $Ca_3Co_4O_9$ thermoelectric properties, J. Alloys Compd. 577 (2013) 511–515.
[35] N. Wu, N.V. Nong, N. Pryds, S. Linderoth, Effects of Yttrium and Iron co-doping on the high temperature thermoelectric properties of $Ca_3Co_4O_{9+\delta}$, J. Alloys Compd. 638 (2015) 127–132.
[36] F.P. Zhang, X. Zhang, Q.M. Lu, J.X. Zhang, Y.Q. Liu, G.Z. Zhang, Effects of Pr doping on thermoelectric transport properties of $Ca_{3-x}Pr_xCo_4O_9$, Solid State Sci. 13 (2011) 1443–1447.
[37] Y. Wang, Y. Sui, J. Cheng, X. Wang, W. Su, H. Fan, Influence of Y^{3+} doping on the high-temperature transport mechanism and thermoelectric response of misfit-layered $Ca_3Co_4O_9$, Appl. Phys. A 99 (2010) 451–458.
[38] P. H Xiang, Y. Kinemuchi, H. Kaga, K. Watari, Fabrication and thermoelectric properties of $Ca_3Co_4O_9$/Ag composites, J. Alloys Compd. 454 (2008) 364–369.
[39] K. Obata, Y. Chonan, T. Komiyama, K. Abe, T. Aoyama, H. Yamaguchi, S. Sugiyama, Thermoelectric properties of $Ca_3Co_4O_9$/$[Ca_2(Co_{0.65}Cu_{0.35})_2O_4]_{0.624}CoO_2$ composites, J. Electron. Mater. 43 (2014) 2425–2429.
[40] S. Butt, W. Xu, M.U. Farooq, G.K. Ren, F. Mohmed, Y. Lin, C.W. Nan, Enhancement of thermoelectric performance in hierarchical mesoscopic oxide composites of $Ca_3Co_4O_9$ and $La_{0.8}Sr_{0.2}CoO_3$, J. Am. Ceram. Soc. 98 (2015) 1230–1235.
[41] C. Boyle, P. Carvillo, Y. Chen, E.J. Barbero, D. McIntyre, X. Song, Grain boundary segregation and thermoelectric performance enhancement of bismuth doped calcium cobaltite, J. Europian Ceramic Society 36 (2016) 601–607.
[42] P. Carvillo, Y. Chen, C. Boyle, P.N. Barnes, X. Song, Thermoelectric performance enhancement of calcium cobaltite through barium grain boundary segregation, Inorg. Chem. 54 (2015) 9027–9032.
[43] C. Boyle, L. Liang, Y. Chen, J. Prucz, E. Cakmak, T.R. Watkins, E.C. Lara, X. Song, Competing dopants grain boundary segregation and resultant seebeck coefficient and power factor enhancement of thermoelectric calcium cobaltite ceramics, Ceram. Int. 43 (2017) 11523–11528.
[44] W.N. Wong, T. Luo, W. Xie, W.H. Tang, J.A. Kaduk, Q. Huang, Y. Yan, S. Chattopadhyay, X. Tang, T. Tritt, Phase diagram, crystal chemistry and thermoelectric properties of compounds in the Ca–Co–Zn–O system, J. Solid State Chem. 184 (2011) 2159–2166.

[45] M. Mikami, N. Ando, R. Funahashi, The effect of Ag addition on electrical properties of the thermoelectric compound $Ca_3Co_4O_9$, J. Solid State Chem. 178 (2005) 2186–2190.
[46] Y. Lu, Y. Song, J. Feng, F.P. Wang, Effects of Ag addition on high temperature thermoelectric properties of $(Ca_{0.9}Gd_{0.1})_3Co_4O_9$ ceramics, Mater. Sci. Forum 650 (2010) 132–136.
[47] G.W. Lee, J.Y. Kim, T. Athar, S.J. Kim, W.S. Seo, K. Park, Electrical conductivity and thermoelectric power studies of solution-combustion-processed $Ca_{2.76}Cu_{0.24}Co_4O_9$, Ceram. Int. 39 (2013) 1397–1402.
[48] Y. Wang, Y. Sui, P. Ren, L. Wang, X. Wang, W. Su, H. Fan, Strongly correlated properties and enhanced thermoelectric response in $Ca_3Co_{4-x}M_xO_9$ (M = Fe, Mn, and Cu), Chem. Mater. 22 (2010) 1155–1163.
[49] A.C. Masset, C. Michel, A. Maignan, M. Hervieu, O. Toulemonde, F. Studer, B. Raveau, J. Hejtmanek, Misfit-layered cobaltite with an anisotropic giant magnetoresistance: $Ca_3Co_4O_9$, Phys. Rev. B 62 (2000) 166–175.
[50] R.R. Heikes, R.C. Miller, R. Mazelsky, Magnetic and electrical anomalies in $LaCoO_3$, Physica 30 (1964) 1600–1608.
[51] S. Yamaguchi, Y. Okimoto, H. Taniguchi, Y. Tokura, Spin-state transition and high-spin polarons in $LaCoO_3$, Phys. Rev. B 53 (1996) R2926–R2929.
[52] M. Abbate, J.C. Fuggle, A. Fujimori, L.H. Tjeng, C.T. Chen, R. Potze, G.A. Sawatzky, H. Eisaki, S. Uchida, Electronic structure and spin-state transition of $LaCoO_3$, Phys. Rev. B 47 (1993) 16124–16130.
[53] S. Yamaguchi, Y. Okimoto, Y. Tokura, Local lattice distortion during the spin-state transition in $LaCoO_3$, Phys. Rev. B 55 (1997) R8666–R8669.
[54] S. Demirel, E. Altin, E. Oz, S. Altin, A. Bayri, An enhancement ZT and spin state transition of $Ca_3Co_4O_9$ with Pb doping, J. Alloys Compd. 627 (2015) 430–437.
[55] S. Altin, M.A. Aksan, A. Bayri, High temperature spin state transitions in misfit-layered $Ca_3Co_4O_9$, J. Alloys Compd. 587 (2014) 40–44.
[56] S.W. Nam, Y.S. Lim, S.M. Choi, W.S. Seo, K. Park, Thermoelectric properties of nanocrystalline $Ca_{3-x}Cu_xCo_4O_9$ ($0 \leq x \leq 0.32$) for power generation, J. Nanosci. 11 (2011) 1734–1737.
[57] R.D. Shannon, C.T. Prewitt, D.B. Rogers, Chemistry of noble metal oxides. II. crystal structures of platinum cobalt dioxide, palladium cobalt dioxide, coppper iron dioxide, and silver iron dioxide, Inorg. Chem. 10 (1971) 719–723.
[58] M. Manickam, V. Ponnuswamy, C. Sankar, R. Suresh, Cobalt oxide thin films prepared by NSP Technique: impact of molar concentration on the structural, optical, morphological and electrical properties, Optik 127 (2016) 5278–5284.
[59] H. Bordeneuve, S.G. Fritsch, A. Rousset, S. Schuurman, V. Poulain, Structure and electrical properties of single-phase cobalt manganese oxide spinels $Mn_{3-x}Co_xO_4$ sintered classically and by spark plasma sintering (SPS), J. Solid State Chem. 182 (2009) 396–401.
[60] C.S. Cheng, M. Serizawa, H. Sakata, T. Hirayama, Electrical conductivity of Co_3O_4 films prepared by chemical vapour deposition, Mater. Chem. Phys. 53 (1998) 225–230.
[61] R.R. Owings, G.J. Exarhos, C.F. Windisch, P.H. Holloway, J.G. Wen, Process enhanced polaron conductivity of infrared transparent nickel–cobalt oxide, Thin Solid Films 483 (2005) 175–184.
[62] F. Delorme, P.D. Chao, E. Guilmeau, F. Giovannelli, Thermoelectric properties of $Ca_3Co_4O_9$–Co_3O_4 composites, Ceram. Int. 41 (2015) 10038–10043.
[63] W. Khan, A.H. Naqvi, M. Gupta, S. Husain, R. Kumar, Small polaron hopping conduction mechanism in Fe doped $LaMnO_3$, J. Chem. Phys. 135 (2011), 054501.
[64] O. Ozdemïr, B. Tatar, D. Yilmazer, P. Gökdemïr, M. Ürgen, K. Kutlu, Alternative approach for determination of energy band gap of semiconductors through electrical analysis, AIP Conf. Proc. 1203 (2010) 875–882.
[65] S. Sindhu, , Sanghi, S.A. Agarwal, V.P. Seth, N. Kishore, Effect of Bi_2O_3 content on the optical band gap, density and electrical conductivity of $MO{\cdot}Bi_2O_3{\cdot}B_2O_3$ (M=Ba, Sr) glasses, Mater. Chem. Phys. 90 (2005) 83–89.
[66] I. Terasaki, I. Tsukada, Y. Iguchi, Impurity-induced transition and impurity-enhanced thermopower in the thermoelectric oxide $NaCo_{2-x}Cu_xO_4$, Phys. Rev. B 65 (2002), 195106.
[67] H.S. Kim, Z.M. Gibbs, Y. Tang, H. Wang, G.J. Snyder, Characterization of lorenz number with seebeck coefficient measurement, Apl. Mater. 3 (2015), 041506.
[68] S. Ballikaya, H. Chi, J.R. Salvador, C. Uher, Thermoelectric properties of Ag-doped Cu_2Se and Cu_2Te, J. Mater. Chem. 1 (2013) 12478–12484.